Retrieval of Global Carbon Dioxide From TanSat Satellite and Comprehensive Validation With TCCON Measurements and Satellite Observations

Xinhua Hong, Peng Zhang, *Senior Member, IEEE*, Yanmeng Bi, Cheng Liu, Youwen Sun, Wei Wang, Zeqing Chen, Hao Yin, Chengxin Zhang, Yuan Tian, and Jianguo Liu

***Abstract*— To cope with global climate change and monitor global CO_2 concentration distribution, the first Chinese carbon dioxide satellite (TanSat) has been successfully launched in December 2016. In this study, we implemented a CO_2 retrieval scheme by calibrating the TanSat sun-glint (GL) mode spectra and adapting the Iterative Maximum *A Posteriori* Differential Optical Absorption Spectroscopy (IMAP-DOAS) algorithm for CO_2 spectral retrieval. The global terrestrial CO_2 total vertical column density (VCD) and column-averaged dry-air mole fractions of CO_2 (X_{CO2}) were simultaneously retrieved from TanSat GL spectral observations. Then, a comprehensive verification was performed between TanSat CO_2 retrieval and other measurements including Total Carbon Column Observing Network (TCCON), the Japanese Greenhouse gases Observing SATellite (GOSAT), and the US Orbiting Carbon Observatory-2 (OCO-2). Further comparisons between our TanSat CO_2 retrieval and ground-based FTIR measurements from TCCON indicated a good correlation with the mean bias of −0.78 ppm, the standard deviation at 1.75 ppm, and the Pearson correlation coefficient of 0.81. In addition, cross-satellite CO_2 validations of TanSat with GOSAT and OCO-2 showed consistently spatiotemporal trends for both CO_2 VCD and X_{CO2}. In summary, we can conclude that the presented CO_2 retrieval scheme has achieved global CO_2 retrieval from TanSat GL mode spectra with high precision and accuracy, as suggested by the results of independent ground-based and satellite validations.**

***Index Terms*— CO_2, Iterative Maximum *A Posteriori* Differential Optical Absorption Spectroscopy (IMAP-DOAS), remote sensing, satellites, spectral analysis, TanSat, X_{CO2}.**

Manuscript received June 29, 2020; revised February 3, 2021; accepted March 13, 2021. Date of publication April 6, 2021; date of current version December 16, 2021. This work was supported in part by the National Natural Science Foundation of China under Grant 41722501, Grant 91544212, Grant 51778596, and Grant 41575021; in part by the Anhui Science and Technology Major Project under Grant 18030801111; in part by the National Key Research and Development Program of China under Grant 2018YFC0213104, Grant 2017YFC0210002, and Grant 2016YFC0203302; in part by the Strategic Priority Research Program of the Chinese Academy of Sciences under Grant XDA23020301; in part by the National Key Project for Causes and Control of Heavy Air Pollution under Grant DQGG0102 and Grant DQGG0205; and in part by the National High-Resolution Earth Observation Project of China under Grant 05-Y30B01–9001-19/20-3. *(Corresponding authors: Peng Zhang; Yanmeng Bi; Cheng Liu.)*

Xinhua Hong is with the School of Environmental Science and Optoelectronic Technology, University of Science and Technology of China, Hefei 230026, China (e-mail: xinhua95@mail.ustc.edu.cn).

Peng Zhang and Yanmeng Bi are with the National Satellite Meteorological Center, China Meteorological Administration, Beijing 100081, China (e-mail: zhangp@cma.gov.cn; biym@cma.cn).

Cheng Liu is with the School of Environmental Science and Optoelectronic Technology, University of Science and Technology of China, Hefei 230026, China, also with the Center for Excellence in Regional Atmospheric Environment, Institute of Urban Environment, Chinese Academy of Sciences, Xiamen 361021, China, also with the Anhui Institute of Optics and Fine Mechanics, Chinese Academy of Sciences, Hefei 230031, China, and also with the Department of Precision Machinery and Precision Instrumentation, University of Science and Technology of China, Hefei 230026, China (e-mail: chliu81@ustc.edu.cn).

Youwen Sun, Wei Wang, Hao Yin, and Jianguo Liu are with the Anhui Institute of Optics and Fine Mechanics, Chinese Academy of Sciences, Hefei 230031, China (e-mail: ywsun@aiofm.ac.cn; wwang@aiofm.ac.cn; yhyh95@mail.ustc.edu.cn; jgliu@aiofm.ac.cn).

Zeqing Chen is with the School of Earth and Space Sciences, University of Science and Technology of China, Hefei 230026, China (e-mail: grateful@mail.ustc.edu.cn).

Chengxin Zhang is with the Department of Precision Machinery and Precision Instrumentation, University of Science and Technology of China, Hefei 230026, China (e-mail: zcx2011@mail.ustc.edu.cn).

Yuan Tian is with the Institutes of Physical Science and Information Technology, Anhui University, Hefei 230601, China, and also with the Anhui Institute of Optics and Fine Mechanics, Chinese Academy of Sciences, Hefei 230031, China (e-mail: ytian@ahu.edu.cn).

Digital Object Identifier 10.1109/TGRS.2021.3066623

I. Introduction

THE Intergovernmental Panel of Climate Change (IPCC) assessment reports have concluded that global warming is already an unquestionable fact. Combined with the global average of land and ocean surface temperature data, the mean temperature has increased at approximately 0.85° from 1880 to 2012 [1], [2]. The main reason for global warming is the greenhouse effect caused by the increasing emissions of greenhouse gases [3]. Among six key greenhouse gases regulated in the Kyoto Protocol, carbon dioxide (CO_2) emissions accounted for 55.46% of the enhanced radiative forcing [2].

Our current knowledge of the carbon cycle is still insufficient given that the existing observation of CO_2 is spatially and temporally limited on the globe. Satellite measurement is an effective approach to monitoring the global distribution of CO_2 at high spatiotemporal resolution [4]. In December 2016, the TanSat satellite was successfully launched by China National Space Administration to better understand the spatial and temporal patterns of sources and sinks of CO_2; it was dedicated to global atmospheric carbon dioxide monitoring [5], [6], similar to its predecessors and successors such as Greenhouse gases Observing SATellite (GOSAT), GOSAT-2 and Orbiting Carbon Observatory (OCO)-2, OCO-3 satellites. The TanSat satellite carried two sensors, i.e., Atmospheric Carbon dioxide Grating Spectroradiometer (ACGS) and Cloud and Aerosol

Polarimetry Imager (CAPI). ACGS can monitor atmospheric oxygen (O_2) and CO_2 concentrations by measuring absorption spectra in three bands, including the molecular O_2 A-band (approximately 758–778 nm, Visible), a weak CO_2 band (approximately 1594–1624 nm, short-wave IR [SWIR]-1), and a strong CO_2 band (approximately 2.042–2.082 nm, SWIR-2) under a spatial resolution of 2 km × 2 km and a spectral resolution of ∼0.044, ∼0.12, and ∼0.16 nm, respectively. CAPI is designed to obtain cloud and aerosol optical characteristics for eliminating cloudy soundings of the ACGS. However, the degradation and instability of the instrument performance have led to the fact that the quality of the TanSat spectra is not as good as its counterparts, such as GOSAT and OCO-2. In previous research (e.g., [6]–[8]), the systematic biases on the instrumental and spectral calibration, as well as their on-orbit degradation were not explicitly considered during TanSat CO_2 retrieval. For example, Wang *et al.* [9] ignored the calibration issue and resulted in a relatively poorer retrieval accuracy of ∼4.16 ppm for TanSat CO_2 before corrected. Recently, the problems were brought to the attention of Yang *et al.* [10]. Then a spectrum correction method was developed by the online fitting of an eighth order Fourier series to solve the spectral problem under the nadir (ND) mode. TanSat sun-glint (GL) mode CO_2 retrievals can provide a great meaningful reference for the aforementioned TanSat products. Meanwhile, complemented on the global scale, the CO_2 retrievals from two measurement modes will be of great significance for understanding and helpful to the application of TanSat products. In fact, the TanSat GL mode spectra seem in a relatively poorer quality than the ND mode spectra (Section III-B). In this study, we recalibrated the TanSat GL spectra to address some unanticipated issues, such as changes in spectral calibration parameters on orbit, low signal-to-noise ratio (SNR) for certain spectral bands, etc., which possibly caused by the instrumental performance changes in the complex space environment after launch. The configuration and parameters of the Iterative Maximum *A Posteriori* (MAP) Differential Optical Absorption Spectroscopy (IMAP-DOAS) algorithm [11] were also adapted for TanSat CO_2 retrieval.

The DOAS technique is an effective approach to determine the total column abundances of trace gases from ground-based [12], satellite [13], [14], and airborne [15] spectroscopy measurements. The classical DOAS approach relies on the linearization of the Lambert–Beer law, where the vertical column density (VCD) to be retrieved is directly proportional to the measured differential optical density [12]. This approach is based on the premise that the absorption cross section of the target gas is independent of temperature and pressure. However, different from in the UV/Vis band, the absorption lines are rather narrow and strongly dependent on temperature and pressure in the near-infrared (NIR) because absorption is only occurred by rotational and vibrational transitions. Therefore, the IMAP-DOAS algorithm has overcome the drawbacks of the DOAS technique in the NIR range. The IMAP-DOAS algorithms have been widely used for satellite CO [16] and CH_4 [17]–[19] retrieval from the SCanning Imaging Absorption spectroMeter for Atmospheric CHartographY (SCIAMACHY), and for verification of other greenhouse gas retrieval algorithms, see [20]–[22].

In this article, we present a CO_2 retrieval scheme and retrieved global CO_2 products from the TanSat sun-GL mode observation. A comprehensive verification was also performed between TanSat CO_2 retrieval and other measurements including TCCON, GOSAT, and OCO-2. This article is organized as follows. Section II presents a brief introduction to the materials. The IMAP-DOAS algorithm, the description of spectral recalibration, and the optimization of the CO_2 retrieval setting to adapt TanSat are described in Section III. Our independent ground-based and satellite validations are presented in Section IV. Section V gives a discussion for the assessment of the optical fit and the limitations of the current retrieval. Finally, Section VI provides a summary.

II. Materials

A. TanSat Data

1) TanSat Level 1B GL Spectra: TanSat was launched on December 21, 2016 with a designed lifetime of three years. Its sun-synchronous orbit height is approximately 700 km. Its revisit period is 16 days with a 13:30 ascending local time. However, the quality of subsequent measurements could not be guaranteed due to the failure of the refrigerant on the satellite since October 2018. Therefore, the available data coverage for strong CO_2 band is the same with that for weak CO_2, i.e., February 2017 to October 2018, and O_2-A band is from February 2017 to present. We used the data from the weak CO_2 band of the GL mode level 1B spectra from March 2017 to September 2018 (available at http://satellite.nsmc.org.cn/portalsite/default.aspx. last accessed on May 22, 2020). Some specific parameters of TanSat-ACGS are shown in Table I [23].

The wavelength associated with each instantaneous field of view (IFOV) footprint per frame in three bands can be described by a six-order polynomial, as follows [24], [25]:

$$\lambda = \sum_{i=0}^{5} C_5 \cdot P^i \tag{1}$$

where λ is the wavelength (nm), P denotes the pixel number, and C_i represents the dispersion coefficient of the ith order.

According to the prelaunch laboratory radiometric calibration of the TanSat-ACGS by the instrument manufacturer, a similar mathematical relation exists between the SNR and radiance in all channels of the three bands, as follows:

$$\mathrm{SNR}(i,j) = \frac{\mathrm{Radiance}(i,j)}{\sqrt{\mathrm{Radiance}(i,j)\cdot C_{1(i,j)}^2 + C_{2(i,j)}^2}} \tag{2}$$

where Radiance *(i,j)* is the apparent radiance of the jth field of view of the ith channel of a certain band. The corresponding SNR curve fitting coefficients are represented by $C_{1(i,j)}$ and $C_{2(i,j)}$.

2) TanSat Cloud Mask Product: The TanSat-CAPI cloud products by Wang *et al.* [26] were used directly for the filtering of satellite ground pixels (the pixels with the cloud mask equaling to 3 were selected). The TanSat-CAPI cloud mask product is reasonably accurate when comparing against

TABLE I
TECHNICAL CHARACTERISTICS OF TANSAT–ACGS

Band	O_2-A	Weak CO_2	Strong CO_2
Spectral coverage (nm)	758–778	1594–1624	2042–2082
Spectral resolution (nm)	0.044	0.12	0.16
Pixels number (spectral dimension × spatial dimension)	1242×9	500×9	500×9
Spatial resolution		2 km × 2 km	
Data coverage	February 2017 to present	February 2017 to October 2018	February 2017 to October 2018

the MODIS cloud-screening product [27], with the Hit Radio (HR) scores > 80% and the Kuiper's skill (KSS) score at ∼0.7 [28].

B. Other Data

1) Solar Irradiance: Due to the degradation and stability of instrument performance, the TanSat mean normalized solar measurement shows change and never gets a radiometric correction. Therefore, we use the high-resolution solar irradiance database provided by R. Kurucz (http://kurucz.harvard.edu/sun/irradiance2008/) to replace TanSat solar measurement as the irradiance. This solar spectrum is measured by high-resolution Fourier Transform Spectrometer (FTS) at the Kitt Peak National Observatory; its wavelength range covers 1560–1740 nm, and the resolution reaches approximately 0.001 nm [4], [29]. We convolve this high-resolution solar spectrum with the recalibrated slit function of TanSat-ACGS SWIR-1 channel to gain I_0, which is mentioned in (3).

2) Profiles and Reference Spectra: Goddard Earth Observing System (GEOS)-Chem model [30] is a global 3-D chemical transport model driven by GEOS-assimilated meteorological fields from the NASA Global Modeling and Assimilation Office [31]. The GEOS-Chem model has many extensive applications in a wide range of research topics on atmospheric composition [32]–[35]. We simulated CO_2, CH_4, H_2O, and dry-air concentrations at the 2° latitude × 2.5° longitude horizontal resolution and 47, 47, 72, and 72 vertical pressure levels. The profiles described mainly involve three atmospheric components with strong absorption at SWIR-1 including CO_2, CH_4, and H_2O. These profiles were interpolated into 10 sublayers, then we used the HIgh-resolution TRANsmission molecular absorption database (HITRAN, Version 2016) [36], [37] and a classical Voigt spectral line shape to calculate CH_4, H_2O, and CO_2 vertical optical densities. In addition, the dry-air profiles were used to calculate the dry-air total VCD.

3) TCCON Data: NIR solar absorption atmospheric measurements by the ground-based FTS of TCCON usually have a very high temporal resolution (∼90 s) and a fine spectral resolution (∼0.02 cm^{-1}) [38], [39]. The retrieval results from TCCON sites are distributed over urban, suburban, rural, and terrain sites worldwide. TCCON has provided an important and independent means of verifying and calibrating satellite measurements. Therefore, the measurements of many appropriate TCCON sites were used to compare with the TanSat X_{CO2} retrievals (available from https://tccondata.org/, last accessed on May 27, 2020).

4) OCO-2 and GOSAT Products: We compared similar products from other satellites to verify the reliability of TanSat CO_2 retrievals including OCO-2 and GOSAT, which are available at https://disc.gsfc.nasa.gov/datasets/and http://data2.gosat.nies.go.jp/, respectively. For the OCO-2 Level 2 standard geo-located CO_2 retrieval results, the version 8r is a previous version of the OCO-2 data set in NASA GES DISK (currently, the latest version is version 10, but its starting date is April 2020) and atmospheric carbon observations from space X_{CO2} retrieval algorithm established and improved by [40] and [41]. The GOSAT Level 2 X_{CO2} products are v02.72 version released by the National Institute for Environmental Studies of Japan. The GOSAT v02.72 version X_{CO2} products are retrieved from the MAP retrieval algorithm improved by [42]. Compared with v01.xx version (bias = −8.85 ppm, standard deviation (SD) = 4.75 ppm) [4], the bias and SD of this version are only −1.48 and 2.09 ppm, respectively, for the validation using TCCON data.

III. RETRIEVAL METHOD

A. IMAP-DOAS Algorithm

The classical DOAS established by [43] can be described as follows:

$$I(\nu) = I_0(\nu)\exp\left(-\int \sigma(\nu)c(s)ds\right) \approx I_0(\nu)\exp\left(-\sigma(\nu)\cdot\int c(s)ds\right), \quad (3)$$

$$\tau = ln\left(\frac{I_0(\nu)}{I(\nu)}\right) \approx \sigma(\nu)\int c(s)ds = \sigma(\nu)\cdot S, \quad (4)$$

$$D(\nu) = S\cdot\sum\nolimits_{i=0}^{n}\sigma_i(\nu)\cdot c_i \quad (5)$$

where $I(\nu)$ represents the radiance received by satellite at the wavelength ν; $I_0(\nu)$ is the irradiance, which is the intensity of solar radiation at wavelength ν. $\sigma(\nu)$ is the absorption cross section of the target gas to be retrieved at wavelength ν. c(s) is the target gas concentration at the optical path s. $D(\nu)$ is the total optical density of n gases at wavelength ν. S denotes the slant column density (SCD), which is defined as the path integral of the concentration of the respective absorber along the actual light path.

In fact, in the NIR wavelength region, the gas absorption cross section has strong temperature- and pressure-dependent properties and varies greatly with wavelength. This finding has been perceived and analyzed by some scientists at the twentieth century to the beginning of this century [44]–[46]. Thus, the drawback of the classical DOAS algorithm under certain

conditions began to be noticed. Then, Buchwitz *et al.* [47] and Rodgers *et al.* [48] made important contributions to solve this problem. The CO_2 retrieval algorithm, namely, the IMAP-DOAS algorithm, is also an improvement on the classical DOAS algorithm. The IMAP-DOAS algorithm has been described in detail by [11] and utilized successfully by [18], [22], [49]–[51], and so on. The sensitivity of atmospheric temperature and pressure profile changes and nonlinear absorption are all considered by this algorithm. In the iterative procedure, the vertical optical densities of the target component are directly simulated and finally achieve the fitting of the differential optical density and the observed spectra. In the classical DOAS approach, some interference between different absorbers or with the Fraunhofer spectrum may occur, but though using convolutions with the instrumental slit function in every iteration, these interferences can be resolved. In addition, simultaneously, the strong absorption effect of the interference component is greatly weakened.

A forward radiative transfer model at high spectral resolution is used to calculate modeled radiance at each wavelength using the following equation:

$$\mathbf{F}(\mathbf{x}_i) = \mathbf{I}_0 \cdot \exp\Big(-\sum \mathbf{A}_n \cdot \boldsymbol{\tau}_n^{\text{ref}} \cdot \mathbf{x}_{n,i}\Big) \cdot \sum_{i=0}^{k} a_k \cdot \lambda^k \tag{6}$$

where $\mathbf{F}(\mathbf{x}_i)$ = the forward modeled radiance at the i-th iteration of the state vector,

$\mathbf{I}_0$ = the incident intensity (solar transmission spectrum),

$\mathbf{A}_n$ = the air mass factor (AMF) for each n number of atmospheric state vector elements,

$\boldsymbol{\tau}_n^{\text{ref}}$ = the reference total optical density for each n number of atmospheric state vector elements,

$\mathbf{x}_{n,i}$ = the trace gas-related state vector at the i-th iteration in each n layers,

a_k = polynomial coefficients to account for low-frequency spectral variations.

According to this equation, optimal estimation is applied with a state vector $\boldsymbol{x}$, which comprises the scaling factors for the prior optical densities of the target trace gases in each vertical atmosphere layer. At each iteration i, a Jacobian matrix $\boldsymbol{K}_{\text{i}}$ is calculated, where each column represents the derivative vector of the observed radiance with respect to each element of the state vector $\boldsymbol{x}_{\text{i}}$ and $\mathbf{K}_i = (\partial \mathbf{F}(\mathbf{x})/\partial \mathbf{x})|_{\mathbf{x}_i}$.

The forward model and the Jacobian matrix can be used to optimize the state vector at the i-th iteration as follows [49]:

$$\mathbf{x}_{i+1} = \mathbf{x}_a + \left(\mathbf{K}_i^T \mathbf{S}_\varepsilon^{-1} \mathbf{K}_i + \mathbf{S}_a^{-1}\right)^{-1} \mathbf{K}_i^T \mathbf{S}_\varepsilon^{-1} \cdot \left[\mathbf{y} - \mathbf{F}(\mathbf{x}_i) + \mathbf{K}_i(\mathbf{x}_i - \mathbf{x}_a)\right] \tag{7}$$

where $\boldsymbol{x}_{\text{a}}$ is a priori state vector, $\boldsymbol{x}_{\text{i}}$ is the atmospheric state vector at the i-th iteration, $\boldsymbol{y}$ is the atmospheric optical density actually measured by the satellite, $\boldsymbol{F}(\boldsymbol{x}_{\text{i}})$ is the forward model evaluated at $\boldsymbol{x}_{\text{i}}$, $\boldsymbol{S}_\varepsilon$ is the error covariance matrix, and $\boldsymbol{S}_{\text{a}}$ is *a priori* covariance matrix.

B. Issues and Improvements

1) Evaluation of the GL Spectra of TanSat: Typically, atmospheric CO_2 abundances vary slightly with respect to the background concentration at ∼400 ppm. Therefore, the retrieval of CO_2 for space-based measurement should have a high precision, indicating that good retrieval conditions are desired. However, many unpredictable issues were exposed and needed to be addressed after TanSat was launched for on-orbit measurements, i.e., low SNR and uncorrected irradiance measurement. Otherwise, the precision accuracy of CO_2 retrieval would be greatly compromised. Furthermore, in the complex space environment (e.g., cosmic radiation exposure and possible instrument changes since launch [52]–[54]), the prelaunch calibration parameters measured in the on-ground laboratory seem unavailable for the TanSat retrieval account for the stability degradation of the instrument.

Unfortunately, we found that these problems are more serious in glint mode than in nadir mode. Two neighbor satellite orbits from the GL and ND, respectively, were used to evaluate the radiance measurement error. As shown in Fig. 1, we have selected three 0.5°× 0.5° regions under a clear sky from the center of Sahara Desert (21° N–26° N, 22° E–27° E). The optical properties atmosphere and land surface could be approximately considered as the same. Thus, the SDs of all spectra at each wavelength inside each box can reflect the measurement error to some extent, i.e., the measured spectra with less error have a smaller SD. The Fig. 1(b)–(d) shows that the GL spectra have an approximately 16% (Area III) to 56% (Area II) higher SDs than ND spectra.

To further illustrate that the TanSat GL spectra are in a relatively poorer quality, TanSat CO_2 retrievals were also performed for ND and GL spectra, respectively, for ground pixels within the terrain region of 30° N–60° N, 45° E–120° E between April 10, 2017 and April 19, 2017 (mostly cloudless overland pixels). In Fig. 2, the left and middle columns show the CO_2 total column from the ND and GL spectra without precalibration, while the results of right column were from the GL spectra with precalibration. The retrieved CO_2 VCDs, root mean square (rms) of fitting residual and retrieval uncertainties are given in panels (a)–(c), panels (d)–(f), and panels (g)–(i), respectively. By comparing Fig. 2(d) and (e), (g) and (h), respectively, both the rms and CO_2 uncertainty from the GL mode were significantly higher than those from the ND mode (rms: 0.075 versus 0.060, Uncertainty: 0.21% versus 0.13%). This result suggested the GL measurement contains much more spectral noise than ND, leading to a challenge for CO_2 retrieval from GL spectra.

2) Spectral Precalibration: In previous trace greenhouse gas retrieval works, such as [18], the high spatial and moderate spectral resolutions were used directly to retrieve target gas concentrations on the basis of the same algorithm, but the TanSat CO_2 retrieval setting should be further optimized. We have conducted a series of targeted tests to improve these conditions, including filtering out poor signal quality, replacing the solar spectrum, fitting wavelength range to avoid low SNR region, and the most important procedure, spectral precalibration.

As shown in Fig. 2(e) and (h), when the GL spectra are not recalibrated, the retrieved rms and uncertainties are in a very high level. To address these issues, we performed an on-orbit

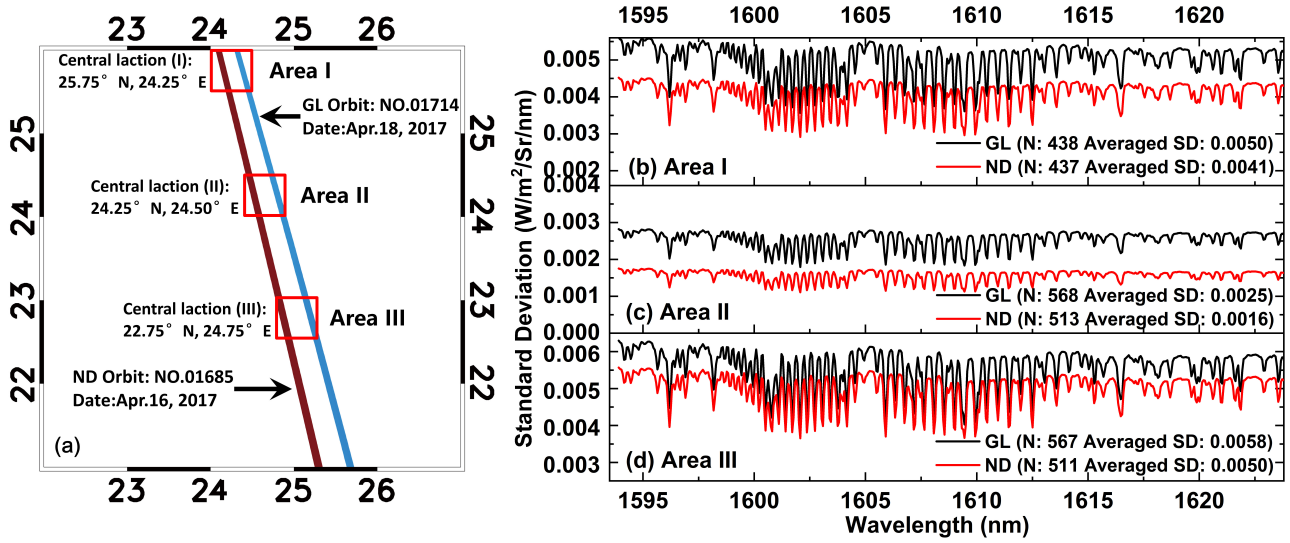

Fig. 1. Comparison of the spectral quality from two neighbor orbits of different observation modes (i.e., GL and ND). (a) Red band represents the orbit 01685 (ND, April 16, 2017) and a blue band represents the orbit 01714 (GL, April 18, 2017). The three selected regions are also shown by the rectangles. (b–d) SDs of the spectra at each wavelength in Area I, II, and III, respectively. The black curves represent the SD form the glint mode, while the red represents the SD from the nadir mode.

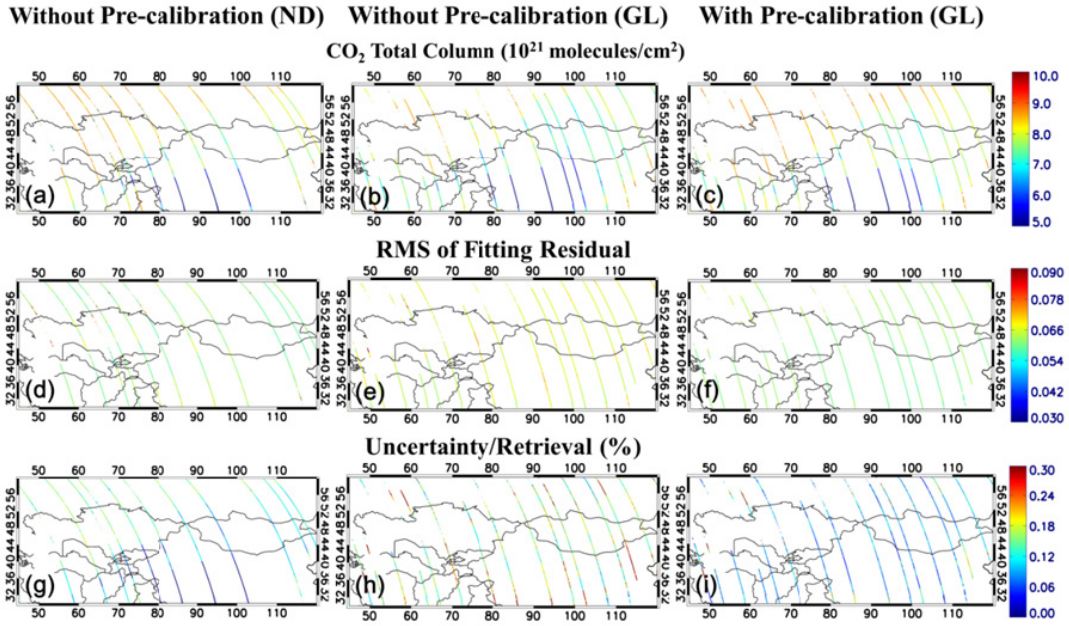

Fig. 2. Comparisons of CO_2 VCD retrieval results from all orbits that passed the region of 30° N–60° N and 45° E–120° E from April 10, 2017 to April 19, 2017. The left and middle columns show the retrieved results from the original [(a), (d), and (g)] ND and [(b), (e), and (h)] GL spectra without precalibration, while the [(c), (f), and (i)] results of right column are from the GL spectra with precalibration. The (a)–(c) retrieved result, (d)–(f) rms of fitting residual, and (g)–(i) uncertainty are placed in the upper, middle, and bottom panels, respectively.

recalibration of the GL spectra. Prior to optical density fitting, some spectral parameters, such as the instrument slit function, spectral shift, and squeeze, were calibrated through cross correlation with a high-resolution solar spectrum. Then the spectral correction factors divided from the retrieval experiment were applied to the linear correction of GL spectra [55]–[58]. The method is described in detail in Appendix A. Fig. 2(c), (f), and (i) represent the retrievals using the current retrieval setting with a spectral precalibration. Compared by Fig. 2(e) and (f), and (h)–(i), evidently, preprocessing the spectra can improve the rms, which is reduced by ∼15%. In addition, the recalibrated measurement spectra lead to a ∼30% decrease in the uncertainty of retrieved total VCD. After recalibrated the spectra, the inversion performance achieved almost close to that in nadir mode.

3) Updates of Configurations and Parameters: Compared to the retrieval of other gases such as CO, CH_4, and HDO based on the IMAP-DOAS algorithm [18], [22], [49]–[51], CO_2 retrieval with the necessary of a 1% (∼4 ppm) precision has more demanding requirements on the related parameters and configurations. The applications of the newer version HITRAN (Version 2016) [37], the corrections of geometrical AMF [59],

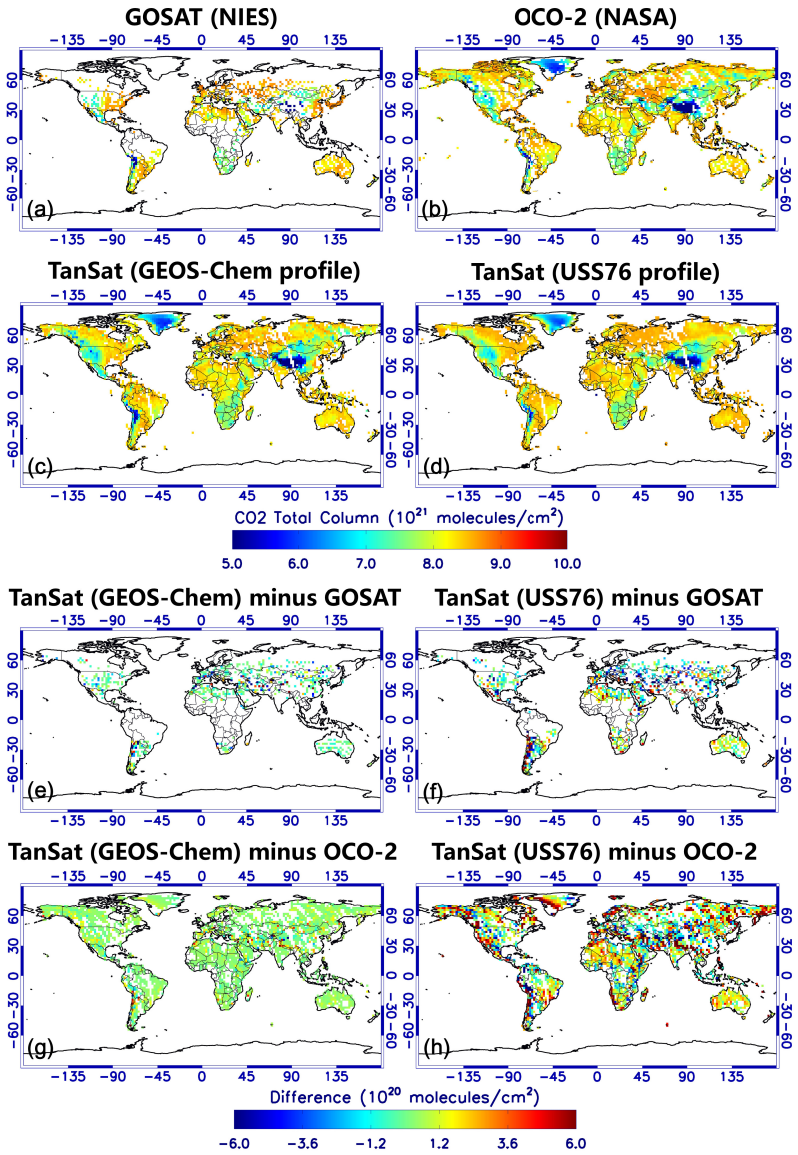

Fig. 3. Sensitivity test about prior profiles on a 2° × 2° grid averaged over April 2017. (a)–(d) Global maps with the CO_2 total VCD of GOSAT, OCO-2, and TanSat products. The products from GOSAT and OCO-2 data sets are placed at (a) and (b), while the retrievals from TanSat using the GEOS-Chem profiles and the USS76 profile are placed at (c) and (d). (e) and (f) Difference between the retrievals of TanSat using the different profiles and GOSAT products. (g) and (h) Same as (e) and (f), but the difference is between TanSat and OCO-2.

and the daily GEOS-Chem priori profiles with a higher spatiotemporal resolution *et al.* have also improved our retrieval accuracy. Table II lists our updated CO_2 retrieval setting, and some configurations and parameters used in [18] are also listed for reference. Take the updating the priori profiles for example, in the previous gas retrieval on the basis of the IMAP-DOAS theory, only a single US standard profile proposed in 1976 (USS76) [60] for target gas *a priori* information at any location all over the world. However, for CO_2 retrieval, the USS76 profile is outdated and not precise enough. Although we have required the degrees of freedom for signal (DFS) for CO_2/X_{CO2} retrieval to be greater than or equal to 1 when filtering, the influence of the priori profiles on the CO_2 retrieval still cannot be ignored. Fig. 3 shows the comparisons of the average CO_2 total VCD on global maps with a 2°× 2° spatial resolution over April 2017 retrieved using different prior profile. Fig. 3(a)–(d) shows the CO_2 retrieval from the GOSAT, OCO-2, and TanSat (with GEOS-Chem and USS76 profiles), respectively. The difference between TanSat retrieval using different prior profiles and the other two satellite data sets is shown in Fig. 3(e)–(h). Apparently, the use of the USS76 priori profile causes a large deference of approximately $-3.6\times10^{20}-6\times10^{20}$ molecules/cm^2, while the application of the GEOS-Chem profiles effectively reduced these differences to within $\pm8\times10^{19}$ molecules/cm^2.

C. Filters

The TanSat data retrieved cover the period from March 10, 2017 to September 30, 2018; 3.164 orbits are available. To improve the accuracy of the retrievals and eliminate the errors caused by cloud, aerosol, large zenith angle, and low SNR in the oceanic region, we have established the following basic screening rules.

TABLE II
UPDATES OF CONFIGURATION AND PARAMETERS

Configurations and parameters	TanSat CO_2 retrieval	AVIRIS CH_4 retrieval [18]
Algorithm	IMAP-DOAS	IMAP-DOAS
Wavelength range	1594–1624 nm	2200–2400 nm
Solar spectrum	R. Kurucz, 2008	Geoffrey Toon, 2013 [61]
Radiometric calibration	Recalibrated radiance	Calibrated radiance
Instrument slit function	Calibrated, Super-Gaussian shape assumed [54].	Preflight measured
Spectral parameters	HITRAN 2016, classical Voigt spectral line shape	HITRAN 2008, classical Voigt spectral line shape
Priori profiles	The daily prior profiles of temperature, pressure, H_2O, CH_4, and CO_2 are obtained from the GEOS-Chem v12-21 at 2°×2.5° for the global domain.	Temperature, pressure, and H_2O volume mixing ratio (VMR) profiles acquired from the NCEP (2.5°×2.5°). CH_4 and N_2O prior profiles are based on the US standard atmosphere.
AMF	1/cos (SZA) + 1/cos (LZA), calculated geometrically with corrections for sphericity adapted from [59].	1/cos (SZA) + 1/cos (LZA)

1) *Only Clear-Sky Scenes:* The entire light path is from the incident point of sunlight entering the atmosphere to the ground footprint corresponding to the measured pixel and then to the satellite receiver. Therefore, we calculate the SCD of CO_2 along this light path in the atmosphere. SCD is related to VCD, the integral of the concentration along the vertical from the surface to the top of the atmosphere, by way of the AMF, where AMF = SCD/VCD. Since scattering in the SWIR is generally low [47], [62], for our applications, if the sky is clear enough, then the impact of scattering is much lower than the retrieval precision error [63]. Thus, scattering in the atmosphere can be neglected, and AMF = 1/cos (SZA) + 1/cos (LZA) (SZA = solar zenith angle, LZA = line-of-sight zenith angle). Then, this geometrical calculation was corrected for sphericity adapted from [59]. However, because clouds are not considered in the IMAP-DOAS algorithm, scattering could become nonnegligible in some scenes, such as heavy aerosol loading, relatively large cloud fraction, or dark surfaces. Similar to [18], considering that the deviation of the AMF may be large under the cloudy or high aerosol weather conditions, we have selected clear scenes to ensure that our retrievals are accurate enough. As for the TanSat-CAPI cloud mask value, specifically, 0 for full cloud, 1 for many clouds, 2 for possible clear sky, and 3 for clear sky. Therefore, to pick out clear-sky scenes, we selected data, where the TanSat-CAPI instrument measured the local cloud mask value equal to 3.
2) *Only Global Land Area*: Relative to the land, due to the ocean surface has low surface reflectance, the SNR is low. Fig. 4 shows one orbit as an example of the measured average SNR and radiance at the weak CO_2 band of every footprint. As shown in Fig. 4, the difference in radiance and SNR between land and ocean areas is very evident. In ocean areas, the average radiance and SNR are only approximately 1/3 of the land area. Furthermore, under a clean cloud-free scene, low radiance and low SNR hinder the accuracy of spectral fitting in ocean areas. On the contrary, under cloudy weather, due to the influence of scattering, a certain inaccuracy is brought to the AMF calculation. Thus, the retrievals in the ocean area still have a large deviation. In view of these reasons, we only selected the global land area as the research object to maximize the retrieval's accuracy.
3) *SZA:* The solar zenith angle $\leq 80°$.
4) *DFS:* DFS for $CO_2 \geq 1$.

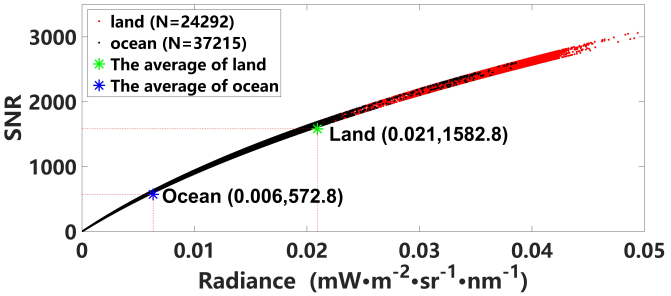

Fig. 4. Scatterplots of the measured SNR and radiance from the whole NO.01262 orbit (date: March 18, 2017) at the weak CO_2 band. The red dots represent land pixels and the black dots represent ocean pixels. The averages of the measured SNR and radiance are included, which of the land and ocean pixels are indicated by a green symbol and a blue symbol, respectively.

IV. RESULTS AND VALIDATIONS

A. Validation Using TCCON Measurements

We used the data from the global TCCON sites for this comparison to validate the TanSat measurements. On the basis of the filter rules described in Section III-C, three additional matching conditions have been added as the spatiotemporal co-location criteria for calculations of the regression analyses as follows [6], [64]–[66].

1) *Spatial Criteria:* All retrievals within 800 km around the site. A relatively wide spatial collocation criteria should be set to obtain sufficient co-incidences due to the narrow swath (∼20 km) and the discrete nature of the observations. Furthermore, this distance is reasonable and feasible because the atmospheric CO_2 abundance is relatively stable.
2) *Temporal Criteria:* Data measured by the TCCON sites within 2 h of the TanSat overpass. We have used the arithmetic mean corresponding to each overpass.
3) *Station Criteria:* We excluded the stations located within areas with significant topography and an active volcano such as Reunion Island or close to source region such as Caltech. Due to Sodankyla and Eureka are at very high latitude, they will also not be used for validation.

TABLE III
SUMMARY OF THE COMPARISON BETWEEN TANSAT RETRIEVALS AND TCCON MEASUREMENTS FOR X_{CO2}

Site	Number	SD (ppm)	Bias (ppm)
Anmyeondo, Korea (ID: an, 36.5382°N, 126.3311°E)	3946	1.59	0.23
Lamont, OK (USA) (ID: oc, 36.604°N, 97.486°W)	467	0.44	0.96
Bremen, Germany (ID: br, 53.10°N, 8.85°E)	5438	1.57	0.73
Izana, Tenerife (ID: iz, 28.3°E, 16.5°W)	4562	1.26	2.66
Karlsruhe, Germany (ID: ka, 49.100°N, 8.439°E)	1203	1.24	-0.54
Lauder, New Zealand (ID: ll, 45.038°S, 169.68°E)	929	1.92	-0.74
Orleans, France (ID: or, 47.97°N, 2.113°E)	1219	0.96	0.66
Park Falls, WI (USA) (ID: pa, 45.945°N, 90.273°W)	1521	1.13	-0.95
Rikubetsu, Japan (ID: ri, 43.4567°N, 143.7661°E)	467	1.19	-0.65
Darwin, Australia (ID: db, 12.424°S, 130.892°E)	3245	1.04	0.85

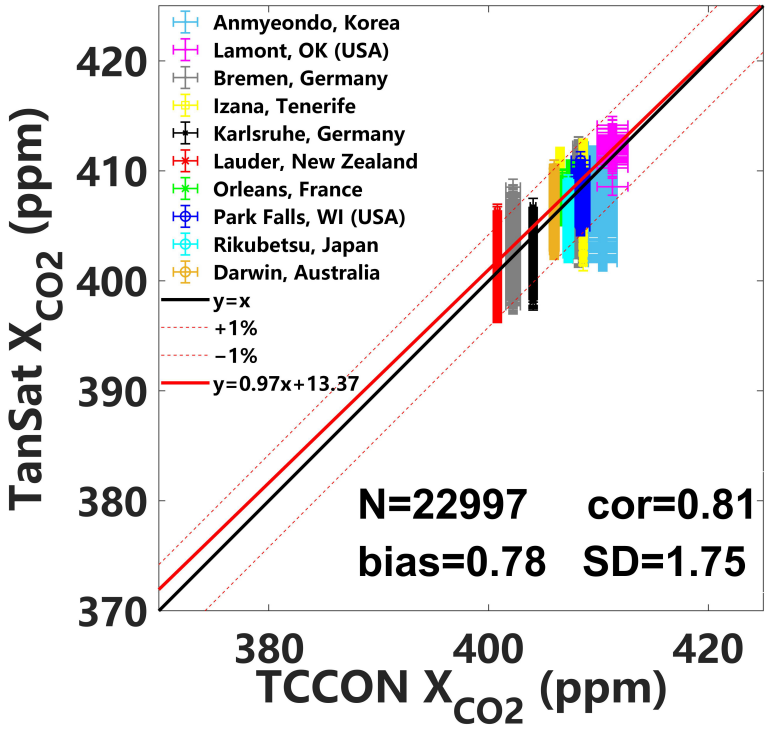

Fig. 5. Correlation analysis of X_{CO2} retrieved from TanSat measurements with collocated TCCON data. Different color and shape symbols indicate different sites in Table III, and the matchups are presented with error bars. Two red dotted lines are used to indicate ±1% deviation and one red line is used to indicate a linear regression fit to the data. The number of matchups (N), the Pearson correlation coefficient (cor), averaged bias, SD, and a black one-to-one line are included.

Under the constraints of these conditions, we compared all the TanSat X_{CO2} retrievals with the global TCCON sites. The average bias and SD between TanSat and TCCON for each site are listed in Table III [67]–[76]. We found that we have maintained good accuracy in comparison with the 10 TCCON sites that satisfied the matching conditions globally. Against most TCCON sites, the SD of TanSat retrievals over land is 0.44 (Lamont) ∼1.59 (Anmyeondo) ppm, and the mean bias derived from the TCCON sites is −0.95 ppm (Park Fall) to +2.66 (Izana) ppm. Most stations have a similar accuracy, which the SD is generally less than 2 ppm, and the mean bias is less than 1 ppm. The correlation analysis corresponding to Table III is shown in Fig. 5. The figure shows, in general, that TanSat retrievals are in good agreement with global TCCON site data. In the overpass averaged results, the bias and SD are 0.78 and 1.75 ppm, respectively. Moreover, the Pearson correlation coefficient is 0.81, and most co-incidences fell in the 1% error region.

B. Validation Using Satellite Observations

Since the launch of the GOSAT and OCO-2, many operational or scientific global CO_2 data sets have been developed from satellite instruments. We performed comparisons with similar products from GOSAT and OCO-2. However, comparing the original retrieved results of individual satellites with each other is especially difficult due to the rare of overlap in spatiotemporal co-locations. Therefore, three satellite products were binned in 2° by 2° grid elements for contrasts and averaged by season.

Fig. 6 shows the global quarterly average CO_2 VCD distribution of TanSat retrievals, GOSAT, and OCO-2 products in the same representative season from September 2017 to August 2018. The distribution of GOSAT retrievals is slightly sparser than the two other satellites but still provides sufficient data for comparison. The content of CO_2 in the atmosphere is very stable. Thus, the CO_2 distribution obtained by the three

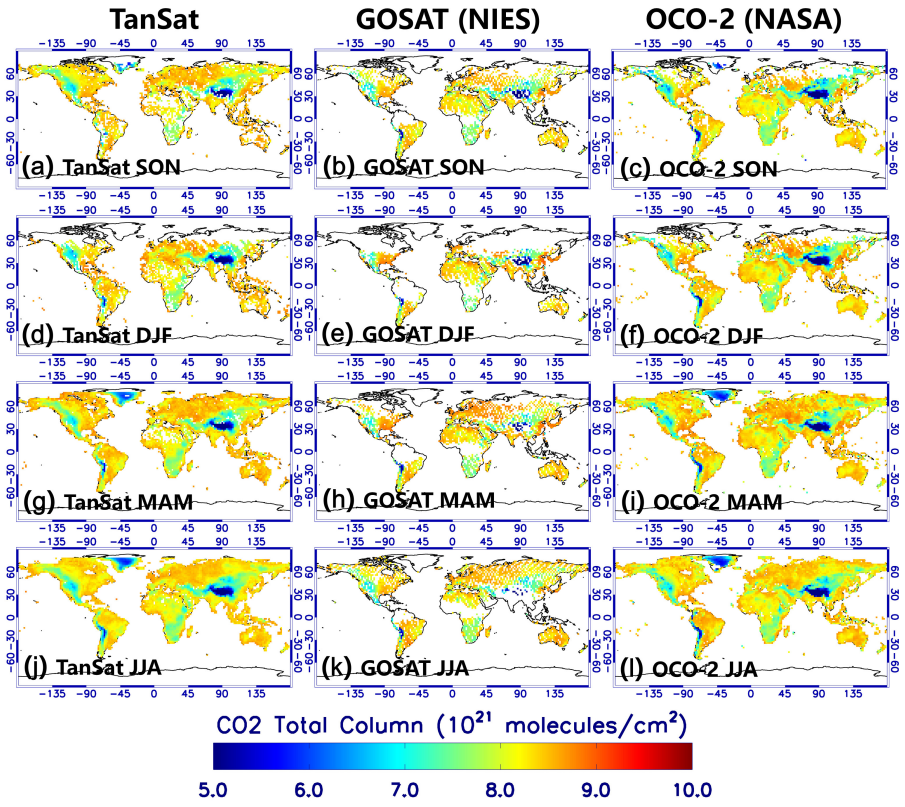

Fig. 6. CO_2 total columns of TanSat, GOSAT, and OCO-2 products are on a $2° \times 2°$ grid averaged by season. The left column is the quarterly average of TanSat retrievals, the middle column belongs to GOSAT, and the OCO-2's products are placed in the right. From top to bottom, the CO_2 total columns are averaged over September 2017 to November 2017, December 2017 to February 2018, March 2018 to May 2018, and June 2018 to August 2018, respectively.

products did not change significantly during the period of one and a half years under study. Evidently, the global CO_2 density has a significant relationship with elevation, and elevation may become the most important influencing factor. Meanwhile, some "hotspots" of CO_2 density are evident, such as around the coastal cities of continents, Europe, Southeast Asia, India, and Southern North America. Large CO_2 emissions are caused by industries and residences due to the intensive and frequent human gathering activities in these regions. Fig. 6 shows that TanSat CO_2 retrieval is highly consistent with the distribution of the two other satellites, particularly in several of the most representative low-value areas, such as the Rocky Mountains in the western North American continent, the Andes in the western South American continent, the South African Plateau, the Himalayas, and most of the Arctic (the Arctic is only compared with OCO-2). For some high-value areas, such as the southeastern continent of North America, northern Latin America, parts of northern Africa, and western Eurasia, TanSat CO_2 total column retrievals are still in good agreements with these satellite products.

Similar to the total column density, global quarterly X_{CO2} composites of TanSat, GOSAT, and OCO-2 are illustrated in Fig. 7 from September 2017 to August 2018. Different from the distribution of total columns, the variation characteristics of global scale X_{CO2} distribution are prominent on time and spatial scales. A fairly high degree of spatiotemporal agreement between the X_{CO2} patterns of three products is found. As shown in Fig. 7, the seasonal variation of X_{CO2} in the southern hemisphere is not as dramatic as the Northern Hemisphere over time. Except for the local winter and spring (from March to August, relative to the southern hemisphere), the other seasons are generally maintained at ~402 ppm over land in the southern hemisphere. However, Fig. 7(g) shows that the TanSat X_{CO2} retrievals are lower than the two other products by approximately ~2 ppm to ~4 ppm in the South African plateau, South America, and Australia. When the southern hemisphere enters its winter [Fig. 7(j)–(l)], to a certain extent, the X_{CO2} values in various regions of the southern hemisphere increase. Relative to its fall, the extent of uplift in the southern hemisphere after entering the winter ranged from TanSat to approximately ~4 ppm to ~8 ppm, and GOSAT and OCO-2 showed values between ~2 and ~6 ppm and ~1 and ~8 ppm, respectively. Fig. 7(j) and (g) showed that this increase is particularly significant in a small number of parts of South Africa and Australia for TanSat data sets.

In fact, whether in the southern hemisphere or the northern hemisphere, X_{CO2} increases in most areas after entering the local winter. This situation in the southern hemisphere has been described in previous paragraph. For the northern hemisphere, in most regions, the values of X_{CO2} have also risen to varying degrees compared with the local autumn. Some studies reported that respiration suppression due to a reduction in snow cover in winter may account for as much as ~25% of the increase in the annual CO_2 sink of northern forests [77]. A decrease in respiration in response to warming during the release period could decrease the amplitude of seasonal CO_2-cycle (SCA) exchange [78].

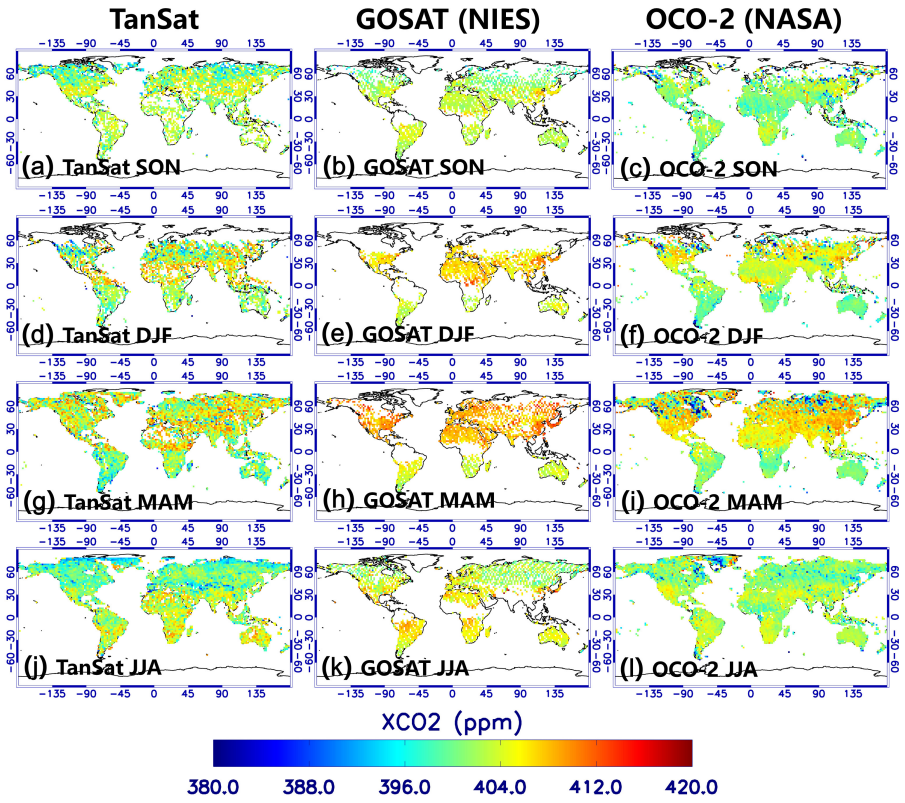

Fig. 7. Same as Fig. 6, but for X_{CO2}.

The land area in the northern hemisphere is more extensive than that of the southern hemisphere, accounting for 67.5% of the total land area of the world. Thus, X_{CO2} distribution becomes comparable. In the local summer and autumn, the hemisphere had been stable at a low value (∼396–398 ppm in most regions). As shown in Fig. 7(a)–(c) and (j) and (k), during this period, the TanSat and OCO-2 evidently have a relatively close appearance, and the GOSAT shows that the regions larger than 400 ppm in northern Africa and Europe are wider and the X_{CO2} values are higher. Figs. 7(d)–(f) and Fig. 7(g)–(i) show that, in the first half of the year after entering winter, the X_{CO2} began to rise to varying degrees in most of the domain until the local spring. Fig. 7(d), (e), (g), and (h) shows that TanSat X_{CO2} retrievals in these regions were at high values (∼405 ppm to ∼412 ppm) throughout the year and had a similar appearance to the GOSAT, especially between 0° to 30°N. However, the OCO-2 products showed smaller X_{CO2} values than the two other products at this latitude band, in the ∼398 ppm to ∼406 ppm range. For higher latitudes, TanSat retrievals were ∼0 ppm to ∼4 ppm lower than GOSAT and OCO-2 data sets in most areas.

To evaluate the reliability of the CO_2 retrieved from TanSat observations, we have compared TanSat retrievals with GOSAT and OCO-2 products as well to quantitatively investigate the reliability of the TanSat CO_2/X_{CO2} products. Before the quantitative comparisons, three products were binned in 2° by 2° grid elements respectively. Then, we selected the grids with the same latitude and longitude on the same day as coincidences. We have matched 976 and 1364 valid coincidences for comparison with GOSAT and OCO-2 data sets, respectively. We performed linear correlation analysis for the CO_2 total column density and X_{CO2}, and the scatter plots against these satellite products are presented in Fig. 8(b), (c), (e), and (f). The same comparison between OCO-2 and GOSAT as a reference is provided in Fig. 8(a) and (d). In general, the following characteristics are apparent from Fig. 8: the linear relationship of CO_2 total column density is better than that of X_{CO2}, and the correlation of OCO-2 products is slightly better than that of GOSAT. Specifically, in terms of the CO_2 VCD, R^2 with GOSAT is 0.73 and that with OCO-2 is 0.75. For X_{CO2}, because the criteria between satellites are not as strict as the comparison with TCCON, R^2 is not as high as the total column amount of CO_2. However, it still reached 0.41 and 0.48, close to the R^2 between the GOSAT and OCO-2. Although the correlation with GOSAT is slightly lower than that with OCO-2, bias and SD are significantly better than the comparison with OCO-2. The mean bias and SD of the former are −2.28 and 2.83 ppm, and those of the latter are 2.65 and 3.48 ppm, respectively.

V. Discussion

A. Assessment of the Fitting Spectra

Following (6) and (7), we used the forward model to fit the optical density, which is the logarithm of the ratio of the standard solar reference spectrum to the radiance from TanSat-ACGS GL mode. Fig. 9 displays an example of simulated optical density in the spectral window of 1605.8–1622.1 nm. Fig. 9(a) shows the optical density of the original and recalibrated spectrum. Fig. 9(b) and (c) shows the spectral

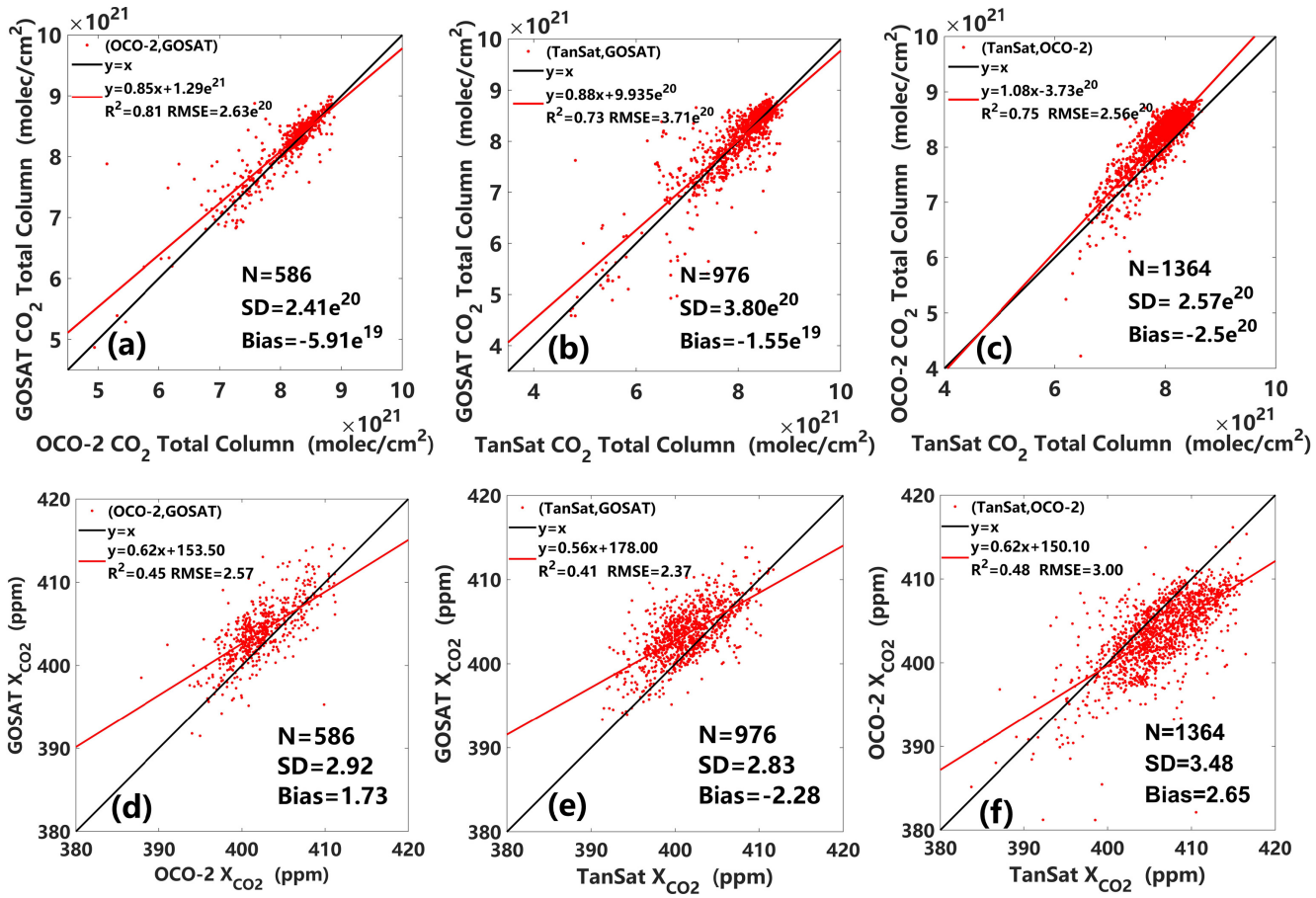

Fig. 8. Scatterplots of the comparisons of the TanSat retrievals against GOSAT and OCO-2 products. (a), (b), and (c) CO_2 total column; (d), (e), and (f) X_{CO2}. In each panel, we provided the number of matchups, the Pearson correlation coefficient R^2, one red line indicated a linear regression fit to the data, one-to-one line, and rms error (RMSE). The number of samples (N), averaged bias, and SD are also included.

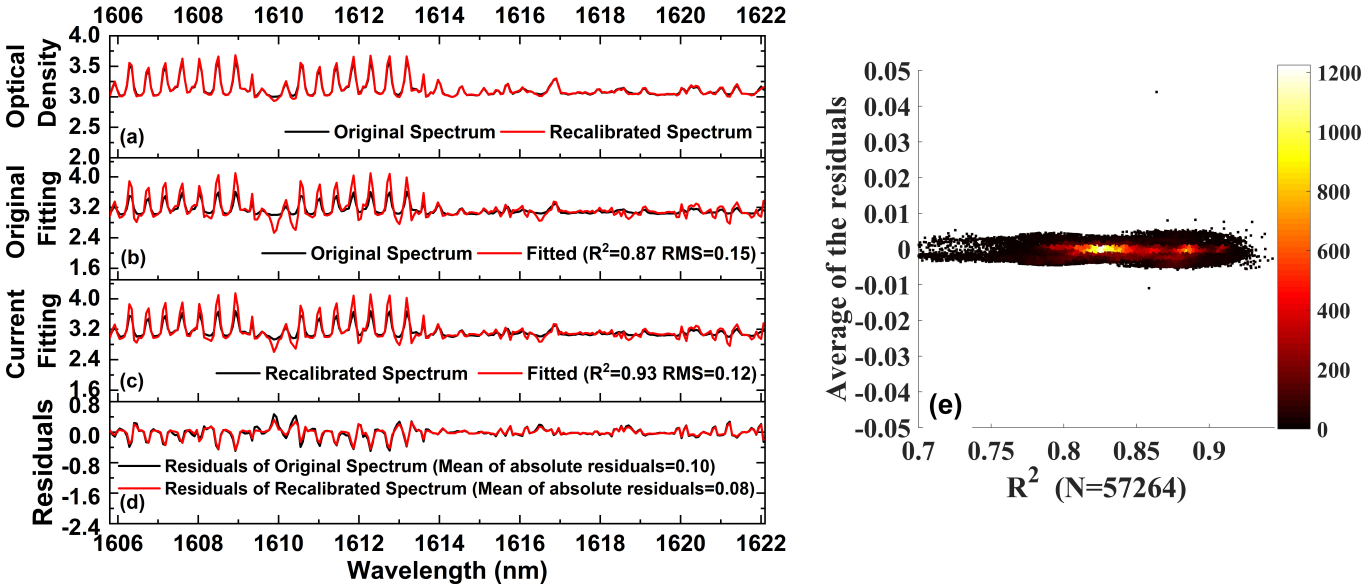

Fig. 9. Spectral fit. (a) Optical density of the original and recalibrated spectra. (b) Fitting of the original spectrum. (c) Same as (b), but for the recalibrated spectrum. (d) Residuals of the fitting in (b) and (c). (e) Density scatterplots for the fit R^2 and average of the residuals from the whole NO.02348 orbit with precalibration.

fitting before and after recalibration. It is visible that the fit differential slant optical density (DSOD) is highly consistent with the measured density in this optical fitting window. The recalibration improved the retrieval of this spectrum, increasing the R^2 from 0.87 to 0.93. Fig. 9(d) has displayed two kinds of residuals (observed optical density minus fit optical density)

of the spectral fittings, which shown in Fig. 9(b) and (c). As Fig. 9(b)–(d) shows, the recalibration greatly improved the retrieval of this spectrum, reducing the rms by 20% and the mean of fit absolute residuals by about 20% for the cited example. Fig. 9(e) shows the distribution of R^2 and the average residuals from the whole NO.02348 orbit. Evidently, after recalibration, for the most fitting results, R^2 is concentrated between ∼0.83 and ∼0.93, and the average residuals are concentrated at ∼ ±0.005.

B. Limitations of the Current Retrieval

The main objective of this study was to retrieve global CO_2 from the TanSat sun-GL mode spectra. Our presented retrieval setting was able to inverse the terrestrial CO_2/X_{CO2} well under a cloudless sky but tended to fail when the cloudy weather or on marine regions. The lower SNR of the spectra in the ocean region and the bias of the geometric AMF due to clouds forced us to abandon the ocean CO_2 retrieval and to choose the definitely cloud-free scenes. With the two major prerequisites of land and clear sky and other filtering conditions described in Section III-C, finally the amount of valid data obtained was only about 11%. Not only for the TanSat, the low percentage of valid data has led to a poor map coverage which seems to have become a major drawback of low-Earth-orbit (LEO) satellites. For example, according to NIES GOSAT Projection (2012) and [65], the percentage of valid data for GOSAT and OCO-2 is less than 5% and approximately 15%, respectively. The low percentage of valid data, long revisit period (∼16 days), narrow swath of TanSat (∼18 km), and the discontinuity of TCCON measurements make it not easy to find sufficient co-incidences for validation against TCCON sites. Fig. 10 and Table IV (in Appendix B) show a validation against TCCON with the spatial criteria of 400 or 550 km. However, there were not enough independent TCCON sites have been involved. Considering the stability of CO_2 in the atmosphere, we finally adopted the spatial criteria of 800 km as [6] for enough matchups. We also retrieved the spectra in nadir mode, and the obtained valid data showed that the percentage was even smaller, only about 8%. As shown in Fig. 11 (Appendix C), the X_{CO2} retrieval results in nadir mode have a lower coverage compared to in glint mode. According to the matching criteria in the A part of Section IV, only two TCCON sites eventually met the validation requirements (JPL, bias = 1.38 ppm, SD = 0.96 ppm [79]; Zugspitze, Germany, bias = 2.80 ppm, SD = 1.28 ppm [80]), leading us to not have enough evidence to determine the precision of the TanSat ND retrievals. We expect that new breakthroughs in algorithms can be achieved in the future to overcome the difficulties of low SNR in marine areas and realize CO_2/X_{CO2} retrieval under higher cloud fraction conditions. Then the CO_2 retrieval using the TanSat L1B spectra will be completer and more sophisticated.

VI. Conclusion

Excellent optical and meteorological conditions are strongly required by the precision of CO_2/X_{CO2} retrieval from satellite measurement. The low signal quality issues of TanSat sun-glint spectra and the retrieval algorithm setting combined with unsuitable configuration and parameters compromise the precision accuracy of CO_2 retrieval. This article presented a method to adapt to TanSat CO_2 retrieval setting and retrieve global CO_2 concentrations through spectral recalibration and the IMAP-DOAS algorithm. We performed a comprehensive verification between TanSat CO_2 retrieval and other measurements including TCCON, GOSAT, and OCO-2. The results proved that the presented retrieval scheme can effectively adapt to TanSat CO_2 retrieval. The time span of the data retrieved was from March 2017 to September 2018. A total of 3.164 available orbits were retrieved for CO_2 total VCD and X_{CO2}, covering all terrestrial regions of the world from 80° S to 80° N under a completely cloudless sky. In the period of approximately one and a half years, we acquired 22.997 available co-incidences with the ten TCCON sites worldwide. The validation against TCCON site data showed that the SD of our measurements can reach 1.75 ppm, and the bias can be within −0.95 ppm to +2.66 ppm. In the correlation analysis, TanSat data sets showed good linear relationship with the GOSAT and OCO-2 data sets. The correlation coefficients R^2 reached 0.73 and 0.75 for the CO_2 total column, and R^2 reached 0.41 and 0.48 for X_{CO2}. In general, the correlation with OCO-2 products was better than that with GOSAT products, and the mean bias and SD of GOSAT were significantly better than those of OCO-2. These comparative results were close to the comparison between GOSAT and OCO-2. Furthermore, the global spatiotemporal distribution of our retrievals showed a high degree of consistency with GOSAT and OCO-2 observations.

Using TanSat data to retrieve CO_2/X_{CO2} has great potential. Next, we will improve our work and attempt to optimize the existing retrievals to seek higher precision and more accurate CO_2/X_{CO2} retrievals in the future.

Appendix A
Assessment of the Fitting Spectra

The instrument response function for the j-th wavelength window, $L_j(\lambda)$, could be fit by a Super-Gaussian shape, which was expressed by the equation

$$L_j(\lambda) = \frac{k}{2\omega\Gamma\left(\frac{1}{k}\right)} \times e^{-\left|\frac{\lambda-\lambda_{c,j}}{\omega}\right|^k} \tag{A1}$$

where ω and k represent the width and shape factors, respectively, while Γ is the gamma function and $\lambda_{c,j}$ represents the center wavelength of the jth wavelength window.

Shift and stretch parameters are permitted to correct possible misalignment between the observed and reference spectra as well as absorption cross sections. A second-order polynomial is used to fit shift and stretch parameters, which was described as

$$\Delta\lambda_j = a + b\left(\lambda_j - \lambda_{c,j}\right) + c\left(\lambda_j - \lambda_{c,j}\right)^2 \tag{A2}$$

where λ_j is the wavelength from the original calibration. The parameters a, b, and c represent the offset and the first and second-order stretch according to λ_j.

Thus, the equation used in the calibration can be expressed as follows:

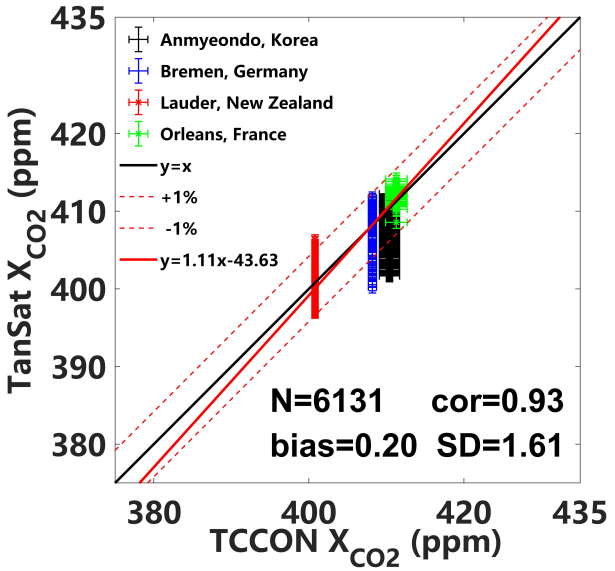

Fig. 10. Same as Fig. 5, but for the spatial criteria of 400 or 550 km.

TABLE IV
SAME AS TABLE III, BUT FOR THE SPATIAL CRITERIA IS OF 400 OR 550 KM

Site	Number	SD (ppm)	Bias (ppm)
Anmyeondo, Korea (ID: an, 36.5382°N, 126.3311°E)	3946	1.82	-0.06
Lamont, OK (USA) (ID: oc, 36.604°N, 97.486°W)	467	-0.99	0.20
Bremen, Germany (ID: br, 53.10°N, 8.85°E)	789	0.46	1.12
Lauder, New Zealand (ID: ll, 45.038°S, 169.68°E)	929	1.92	-0.74

$$I'(\lambda) = (I_S \otimes L)(\lambda - \Delta\lambda) \times \exp\left(-\sum_{i=1}^{n} c_i(\sigma_i \otimes L)(\lambda - \Delta\lambda)\right) \quad \text{(A3)}$$

where $I'(\lambda)$ is the spectrum with recalibration, $I_S(\lambda)$ is the solar spectrum with a high wavelength resolution, $\otimes$ is the convolution symbol, c_i is the column density of the species i, and σ_i is the absorption cross section of the species i.

To correct the spectra, we performed a retrieval experiment. The simulated spectrum at the retrieval experiment $I_{\text{sim}}(\lambda)$ was divided by its $I'(\lambda)$ to obtain the spectral correction factor $\text{cor}(\lambda)$, which was described as

$$\text{cor}(\lambda) = \frac{I_{\text{sim}}(\lambda)}{I'(\lambda)}. \quad \text{(A4)}$$

6432 groups of correction factors were given in the retrieval experiment. These correction factors were averaged at each wavelength to obtain the final correction factors $\text{cor}_{\text{avg}}(\lambda)$, which were applied to the linear correction of all spectra. Thus, the original spectrum was recalibrated and convert to the $\text{cor}_{\text{avg}}(\lambda) \cdot I'(\lambda)$, which was used to the actual retrieval.

APPENDIX B
VALIDATION AGAINST TCCON WITH OTHER SPATIAL CRITERIA

See Fig. 10 and Table IV.

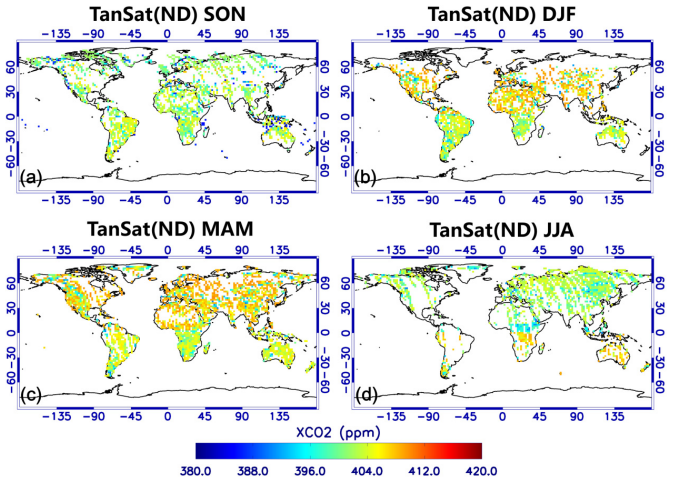

Fig. 11. X_{CO2} retrieved from the TanSat nadir mode spectra on a 2°× 2° grid averaged by season.

TABLE V
SAME AS TABLE III, BUT FOR THE TANSAT CO_2 RETRIEVAL FROM ND SPECTRA

Site	Number	SD (ppm)	Bias (ppm)
Zugspitze, Germany (ID: zs, 47.42°N, 10.98°E)	3464	1.28	2.80
JPL (ID: jf, 34.202°N, 118.175°W)	2494	0.96	1.38

APPENDIX C
TANSAT CO_2 RETRIEVAL FROM ND SPECTRA

See Fig. 11 and Table V.

ACKNOWLEDGMENT

The authors thank the TCCON and PIs for providing ground-based X_{CO2} data: Tae-Young Goo (PI of Anmyeondo), Paul Wennberg (PI of Lamont and Park Falls), Justus Notholt (PI of Bremen), Thomas Blumenstock (PI of Izana), Frank Hase (PI of Karlsruhe), Dave Pollard (PI of Lauder), Isamu Morino (PI of Rikubetsu), Nicholas Deutscher (IP of Darwin), R. Sussmann (IP of Zugspitze), Debra Wunch, Young-Suk oh and Voltaire A. Velazco, Christof Petri, Matthias Schneider, S. Dohe, Vanessa Sherlock, J. Messerschmidt, Rebecca A. Washenfelder, DavidW.T. Griffith, Coleen Roehl, J.-F. Blavier, Geoffrey C. Toon, M. Rettinger, and every person working in TCCON. They thank Xi Wang, Zheng Guo, Yipeng Huang, Hongjie Fan, and Wanbiao Li for the TanSat-CAPI cloud mask products. They thank the OCO-2 team and the GOSAT team for providing satellite products. They are also deeply indebted to Nicholas Deutscher (Centre for Atmospheric Chemistry, School of Chemistry, University of Wollongong) and Dr. Lianghai Wu (SRON Netherlands Institute for Space Research, Utrecht, the Netherlands) for their helpful comments and suggestions during the preparation of this article. They would also like to thank the two anonymous reviewers for their insightful comments, which helped to improve the article significantly.

REFERENCES

[1] (IPCC) Report. (2007). *Intergovernmental Panel of Climate Change*. [Online]. Available: https://www.ipcc.ch/report/ar4/syr/

[2] (IPCC) Report. (2014). *Intergovernmental Panel of Climate Change*. [Online]. Available: https://www.ipcc.ch/report/ar5/syr/

[3] N. Jones, "Troubling milestone for CO_2," *Nature Geosci.*, vol. 6, no. 8, p. 589, 2013.

[4] Y. Yoshida *et al.*, "Retrieval algorithm for CO_2 and CH_4 column abundances from short-wavelength infrared spectral observations by the Greenhouse gases observing satellite," *Atmos. Meas. Techn.*, vol. 4, no. 4, pp. 717–734, 2011.

[5] Y. Liu, Z. Cai, D. Yang, Y. Zheng, M. Duan, and D. Lü, "Effects of spectral sampling rate and range of CO_2 absorption bands on XCO_2 retrieval from TanSat hyperspectral spectrometer," *Chin. Sci. Bull.*, vol. 59, no. 14, pp. 1485–1491, May 2014.

[6] Y. Liu *et al.*, "The TanSat mission: Preliminary global observations," *Sci. Bull.*, vol. 63, no. 18, pp. 38–45, 2018.

[7] D. Yang, Y. Liu, Z. Cai, X. Chen, L. Yao, and D. Lu, "First global carbon dioxide maps produced from TanSat measurements," *Adv. Atmos. Sci.*, vol. 35, no. 6, pp. 621–623, Jun. 2018.

[8] Y. Liu, D. Yang, and Z. Cai, "A retrieval algorithm for TanSat XCO_2 observation: Retrieval experiments using GOSAT data," *Chin. Sci. Bull.*, vol. 58, no. 13, pp. 1520–1523, May 2013.

[9] S. Wang *et al.*, "Carbon dioxide retrieval from TanSat observations and validation with TCCON measurements," *Remote Sens.*, vol. 12, no. 14, p. 2204, Jul. 2020.

[10] D. Yang *et al.*, "Toward high precision XCO_2 retrievals from TanSat observations: Retrieval improvement and validation against TCCON measurements," *J. Geophys. Res., Atmos.*, vol. 125, no. 22, 2020, Art. no. e2020JD032794.

[11] C. Frankenberg, U. Platt, and T. Wagner, "Iterative maximum *a posteriori* (IMAP)-DOAS for retrieval of strongly absorbing trace gases: Model studies for CH_4 and CO_2 retrieval from near infrared spectra of SCIAMACHY onboard ENVISAT," *Atmos. Chem. Phys.*, vol. 5, no. 1, pp. 9–22, 2005.

[12] J. Stutz *et al.*, "Simultaneous DOAS and mist-chamber IC measurements of HONO in Houston, TX," *Atmos. Environ.*, vol. 44, no. 33, pp. 4090–4098, Oct. 2010.

[13] O. Schneising *et al.*, "Atmospheric greenhouse gases retrieved from SCIAMACHY: Comparison to ground-based FTS measurements and model results," *Atmos. Chem. Phys.*, vol. 12, no. 3, pp. 1527–1540, Feb. 2012.

[14] C. Zhang *et al.*, "Satellite UV-Vis spectroscopy: Implications for air quality trends and their driving forces in China during 2005-2017," *Light, Sci. Appl.*, vol. 8, no. 1, p. 100, Nov. 2019.

[15] K. Gerilowski *et al.*, "MAMAP—A new spectrometer system for column-averaged methane and carbon dioxide observations from aircraft: Instrument description and performance analysis," *Atmos. Meas. Techn.*, vol. 4, no. 2, pp. 215–243, Feb. 2011.

[16] C. Frankenberg, U. Platt, and T. Wagner, "Retrieval of CO from SCIAMACHY onboard ENVISAT: Detection of strongly polluted areas and seasonal patterns in global CO abundances," *Atmos. Chem. Phys.*, vol. 5, no. 6, pp. 1639–1644, Jun. 2005.

[17] C. Frankenberg *et al.*, "Global column-averaged methane mixing ratios from 2003 to 2009 as derived from SCIAMACHY: Trends and variability," *J. Geophys. Res., Atmos.*, vol. 116, no. D04302, 2011, doi: 10.1029/2010JD014849.

[18] A. K. Thorpe, C. Frankenberg, and D. A. Roberts, "Retrieval techniques for airborne imaging of methane concentrations using high spatial and moderate spectral resolution: Application to AVIRIS," *Atmos. Meas. Techn.*, vol. 7, no. 2, pp. 491–506, Feb. 2014.

[19] A. K. Thorpe *et al.*, "Airborne DOAS retrievals of methane, carbon dioxide, and water vapor concentrations at high spatial resolution: Application to AVIRIS-NG," *Atmos. Meas. Techn.*, vol. 10, no. 10, pp. 3833–3850, Oct. 2017.

[20] S. Oshchepkov, A. Bril, and T. Yokota, "PPDF-based method to account for atmospheric light scattering in observations of carbon dioxide from space," *J. Geophys. Res., Atmos.*, vol. 113, no. D23210, 2008, doi: 10.1029/2008JD010061.

[21] A. K. Petersen *et al.*, "First ground-based FTIR observations of methane in the inner tropics over several years," *Atmos. Chem. Phys.*, vol. 10, no. 15, pp. 7231–7239, Aug. 2010.

[22] Z. Tan *et al.*, "Inverse modeling of pan-arctic methane emissions at high spatial resolution: What can we learn from assimilating satellite retrievals and using different process-based wetland and lake biogeochemical models?" *Atmos. Chem. Phys.*, vol. 16, no. 19, pp. 12649–12666, Oct. 2016.

[23] S. Du *et al.*, "Retrieval of global terrestrial solar-induced chlorophyll fluorescence from TanSat satellite," *Sci. Bull.*, vol. 63, no. 22, pp. 1502–1512, Nov. 2018.

[24] Z. Yang *et al.*, "Laboratory spectral calibration of the TanSat atmospheric carbon dioxide grating spectrometer," *Geosci. Instrum., Methods Data Syst.*, vol. 7, no. 3, pp. 245–252, Aug. 2018.

[25] Z. Yang *et al.*, "Prelaunch radiometric calibration of the TanSat atmospheric carbon dioxide grating spectrometer," *IEEE Trans. Geosci. Remote Sens.*, vol. 56, no. 7, pp. 4225–4233, Jul. 2018.

[26] X. Wang, Z. Guo, Y. Huang, H. Fan, and W. Li, "A cloud detection scheme for the Chinese carbon dioxide observation satellite (TANSAT)," *Adv. Atmos. Sci.*, vol. 34, no. 1, pp. 16–25, Jan. 2017.

[27] S. Ackerman and R. Frey, "MODIS atmosphere L_2 cloud mask product," NASA MODIS Adapt. Process. Syst., Goddard Space Flight Center, Greenbelt, MD, USA, 2015.

[28] K.-G. Karlsson and A. Dybbroe, "Evaluation of arctic cloud products from the EUMETSAT climate monitoring satellite application facility based on CALIPSO-CALIOP observations," *Atmos. Chem. Phys.*, vol. 10, no. 4, pp. 1789–1807, Feb. 2010.

[29] R. L. Kurucz, "High resolution irradiance spectrum from 300 to 1000 nm," presented at the AFRL Transmiss. Meeting, Lexington, MA, USA, Jun. 2005. [Online]. Available: https://ui.adsabs.harvard.edu/abs/2006astro.ph..5029K/abstract

[30] I. Bey *et al.*, "Global modeling of tropospheric chemistry with assimilated meteorology: Model description and evaluation," *J. Geophys. Res., Atmos.*, vol. 106, no. D19, pp. 23073–23095, Oct. 2001.

[31] K. L. Chan and K. L. Chan, "Aerosol optical depths and their contributing sources in taiwan," *Atmos. Environ.*, vol. 148, pp. 364–375, Jan. 2017.

[32] E. W. Emerson *et al.*, "Revisiting particle dry deposition and its role in radiative effect estimates," *Proc. Nat. Acad. Sci. USA*, vol. 117, no. 42, pp. 26076–26082, Oct. 2020.

[33] H. Yin *et al.*, "Ground-based FTIR observation of hydrogen chloride (HCl) over Hefei, China, and comparisons with GEOS-chem model data and other ground-based FTIR stations data," *Opt. Exp.*, vol. 28, no. 6, p. 8041, 2020.

[34] X. Liu *et al.*, "High levels of daytime molecular chlorine and nitryl chloride at a rural site on the north China plain," *Environ. Sci. Technol.*, vol. 51, no. 17, pp. 9588–9595, Sep. 2017.

[35] E. Lutsch *et al.*, "Detection and attribution of wildfire pollution in the arctic and northern midlatitudes using a network of Fourier-transform infrared spectrometers and GEOS-chem," *Atmos. Chem. Phys.*, vol. 20, no. 21, pp. 12813–12851, Nov. 2020.

[36] L. S. Rothman *et al.*, "The HITRAN2012 molecular spectroscopic database," *J. Quant. Spectrosc. Radiat. Transf.*, vol. 130, pp. 4–50, Nov. 2013.

[37] I. E. Gordon *et al.*, "The HITRAN2016 molecular spectroscopic database," *J. Quant. Spectrosc. Radiat. Transf.*, vol. 203, pp. 3–69, Dec. 2017.

[38] D. Wunch, G. C. Toon, S. C. Wofsy, B. B. Stephens, and P. O. Wennberg, "A calibration for the total carbon column observing network using HIPPO aircraft profiles," in *Proc. AGU Fall Meeting Abstr.*, 2009, p. A44A-02.

[39] D. Wunch *et al.*, "The total carbon column observing network," *Philos. Trans. Roy. Soc. A, Math., Phys. Eng. Sci.*, vol. 369, pp. 2087–2112, May 2011.

[40] C. W. O'Dell *et al.*, "The ACOS CO_2 retrieval algorithm—Part 1: Description and validation against synthetic observations," *Atmos. Meas. Tech.*, vol. 5, no. 1, pp. 99–121, 2012.

[41] C. W. O'Dell *et al.*, "Improved retrievals of carbon dioxide from Orbiting Carbon Observatory-2 with the version 8 ACOS algorithm," *Atmos. Meas. Techn.*, vol. 11, no. 12, pp. 6539–6576, Dec. 2018.

[42] Y. Yoshida *et al.*, "Improvement of the retrieval algorithm for GOSAT SWIR XCO_2 and XCH_4 and their validation using TCCON data," *Atmos. Meas. Techn.*, vol. 6, no. 6, pp. 1533–1547, 2013.

[43] U. Platt and J. Stutz, *Differential Optical Absorption Spectroscopy*. Hoboken, NJ, USA: Wiley, 2006, pp. 135–158.

[44] S. Solomon *et al.*, "Atmospheric NO3: 1. Measurement technique and the annual cycle at 40°N," *J. Geophys. Res.*, vol. 94, no. D8, pp. 11041–11048, 1989.

[45] R. Volkamer, "Correction of the oxygen interference with UV spectroscopic (DOAS) measurements of monocyclic aromatic hydrocarbons in the atmosphere," *Atmos. Environ.*, vol. 32, no. 21, pp. 3731–3747, Nov. 1998.

[46] A. N. Maurellis, R. Lang, and W. J. van der Zande, "A new DOAS parameterization for retrieval of trace gases with highly-structured absorption spectra," *Geophys. Res. Lett.*, vol. 27, no. 24, pp. 4069–4072, Dec. 2000.

[47] M. Buchwitz, R. de Beek, S. Noél, H. Bovensmann, and J. P. Burrows, "Retrieval of CO, H_2O, CH_4, CO_2, and N_2O columns from SCIAMACHY/Envisat by WFM-DOAS: Current status," in *Proc. Envisat ERS Symp.*, vol. 572, 2005, p. 132.1.
[48] C. D. Rodgers, *Inverse Methods for Atmospheric Sounding*. Singapore: World Scientific, 2000.
[49] C. Frankenberg *et al.*, "Dynamic processes governing lower-tropospheric HDO/H_2O ratios as observed from space and ground," *Science*, vol. 325, no. 5946, p. 1374, 2009.
[50] C. Frankenberg *et al.*, "Airborne methane remote measurements reveal heavy-tail flux distribution in Four Corners region," *Proc. Nat. Acad. Sci. USA*, vol. 113, no. 35, pp. 9734–9739, Aug. 2016.
[51] R. A. Scheepmaker *et al.*, "Validation of SCIAMACHY HDO/H_2O measurements using the TCCON and NDACC-MUSICA networks," *Atmos. Meas. Techn.*, vol. 8, no. 4, pp. 1799–1818, 2015.
[52] M. Zhao *et al.*, "Effect of AO/UV/RD exposure on spaceborne diffusers: A comparative experiment," *Appl. Opt.*, vol. 54, no. 31, p. 9157, 2015.
[53] V. M. E. Schenkeveld *et al.*, "In-flight performance of the ozone monitoring instrument," *Atmos. Meas. Techn.*, vol. 10, no. 5, pp. 1957–1986, Jun. 2017.
[54] C. Zhang *et al.*, "Preflight evaluation of the performance of the chinese environmental trace gas monitoring instrument (EMI) by spectral analyses of nitrogen dioxide," *IEEE Trans. Geosci. Remote Sens.*, vol. 56, no. 6, pp. 3323–3332, Jun. 2018.
[55] K. Chance and R. L. Kurucz, "An improved high-resolution solar reference spectrum for Earth's atmosphere measurements in the ultraviolet, visible, and near infrared," *J. Quant. Spectrosc. Radiat. Transf.*, vol. 111, no. 9, pp. 1289–1295, Jun. 2010.
[56] C. Zhang *et al.*, "First observation of tropospheric nitrogen dioxide from the environmental trace gases monitoring instrument onboard the GaoFen-5 satellite," *Light, Sci. Appl.*, vol. 9, no. 1, Dec. 2020.
[57] X. Liu, P. K. Bhartia, K. Chance, R. J. D. Spurr, and T. P. Kurosu, "Ozone profile retrievals from the ozone monitoring instrument," *Atmos. Chem. Phys.*, vol. 10, no. 5, pp. 2521–2537, Mar. 2010.
[58] J. Bak *et al.*, "Characterization and correction of OMPS nadir mapper measurements for ozone profile retrievals," *Atmos. Meas. Techn.*, vol. 10, no. 11, pp. 4373–4388, Nov. 2017.
[59] F. Kasten and A. T. Young, "Revised optical air mass tables and approximation formula," *Appl. Opt.*, vol. 28, no. 22, pp. 4735–4738, 1989.
[60] F. X. Kniezys *et al.*, "The MODTRAN 2/3 report and LOWTRAN 7 model," L. W. Abreu and G. P. Anderson, Eds., Phillips Lab., Geophys. Directorate, PL/GPOS, Hanscom AFB, MA, USA, Nov. 1996. [Online]. Available: http://web.gps.caltech.edu/~vijay/pdf/modrept.pdf
[61] G. Toon, "FTS measurements of the solar spectrum," Jet Propuls. Lab., California Inst. Technol., Pasadena, CA, USA, Tech. Rep. FTh1C.3, 2013. [Online]. Available: https://www.osapublishing.org/abstract.cfm?URI=FTS-2013-FTh1C.3, doi: 10.1364/FTS.2013.FTh1C.3.
[62] E. Dufour and F.-M. Bréon, "Spaceborne estimate of atmospheric CO_2 column by use of the differential absorption method: Error analysis," *Appl. Opt.*, vol. 42, no. 18, pp. 3595–3609, 2003.
[63] J. Mao and S. R. Kawa, "Sensitivity studies for space-based measurement of atmospheric total column carbon dioxide by reflected sunlight," *Appl. Opt.*, vol. 43, no. 4, pp. 914–927, 2004.
[64] M. Zhou *et al.*, "Validation of TANSO-FTS/GOSAT XCO_2 and XCH_4 glint mode retrievals using TCCON data from near-ocean sites," *Atmos. Meas. Tech.*, vol. 9, no. 3, pp. 1415–1430, 2016.
[65] L. Wu *et al.*, "Carbon dioxide retrieval from OCO-2 satellite observations using the RemoTeC algorithm and validation with TCCON measurements," *Atmos. Meas. Techn.*, vol. 11, no. 5, pp. 3111–3130, May 2018.
[66] Y. Bi, Q. Wang, Z. Yang, J. Chen, and W. Bai, "Validation of column-averaged dry-air mole fraction of CO_2 retrieved from OCO-2 using ground-based FTS measurements," *J. Meteorological Res.*, vol. 32, no. 3, pp. 433–443, Jun. 2018.
[67] T.-Y. Goo, Y.-S. Oh, and V. A. Velazco. (2014). *TCCON Data From Anmeyondo (KR), Release GGG2014.R0*. [Online]. Available: https://data.caltech.edu/records/266
[68] P. O. Wennberg, D. Wunch, C. M. Roehl, J.-F. Blavier, G. C. Toon, and N. T. Allen. (2016). *TCCON Data From Lamont (US), Release GGG2014.R1*. [Online]. Available: https://data.caltech.edu/records/279
[69] J. Notholt *et al.* (2014). *TCCON Data From Bremen (DE), Release GGG2014.R0*. [Online]. Available: https://data.caltech.edu/records/268
[70] T. Blumenstock, F. Hase, M. Schneider, O. E. García, and E. Sepúlveda. (2017). *TCCON Data From Izana (ES), Release GGG2014.R1*. [Online]. Available: https://data.caltech.edu/records/302
[71] F. Hase, T. Blumenstock, S. Dohe, J. Groß, and M. Kiel. (2015). *TCCON Data From Karlsruhe (DE), Release GGG2014.R1*. [Online]. Available: https://data.caltech.edu/records/278
[72] V. Sherlock, B. Connor, J. Robinson, H. Shiona, D. Smale, and D. F. Pollard. (2014). *TCCON Data From Lauder (NZ), 125HR, Release GGG2014.R0*. [Online]. Available: https://data.caltech.edu/records/281.
[73] T. Warneke *et al.* (2019). *TCCON Data From Orléans (FR), Release GGG2014.R1*. [Online]. Available: https://data.caltech.edu/records/1301.
[74] P. O. Wennberg *et al.* (2017). *TCCON Data From Park Falls (US), Release GGG2014.R1*. [Online]. Available: https://data.caltech.edu/records/295
[75] I. Morino, N. Yokozeki, T. Matsuzaki, and M. Horikawa. (2016). *TCCON Data From Rikubetsu (JP), Release GGG2014.R1*. [Online]. Available: https://data.caltech.edu/records/287
[76] D. W. T. Griffith *et al.* (2014). *TCCON Data From Darwin (AU), Release GGG2014.R0*. [Online]. Available: https://data.caltech.edu/records/269
[77] Z. Yu *et al.*, "Decrease in winter respiration explains 25% of the annual northern forest carbon sink enhancement over the last 30 years," *Global Ecol. Biogeography*, vol. 25, no. 5, pp. 586–595, 2016.
[78] A. Bastos *et al.*, "Contrasting effects of CO_2 fertilization, land-use change and warming on seasonal amplitude of Northern Hemisphere CO_2 exchange," *Atmospheric Chem. Phys.*, vol. 19, no. 19, pp. 12361–12375, 2019.
[79] P. O. Wennberg *et al.* (2016). TCCON data from jet propulsion laboratory (US), Release GGG2014.R1. [Online]. Available: https://data.caltech.edu/records/277
[80] R. Sussmann and M. Rettinger. (2018). TCCON data from Zugspitze (DE), Release GGG2014.R1. [Online]. Available: https://data.caltech.edu/records/923

Xinhua Hong received the B.E. degree in hydrology and water resources engineering from Sichuan University, Chengdu, China, in 2018. He is pursuing the Ph.D. degree with the School of Environmental Science and Optoelectronic Technology, University of Science and Technology of China, Hefei, China.

His research interest includes the satellite retrieval of atmospheric greenhouse gases.

Peng Zhang (Senior Member, IEEE) received the master's degree in atmospheric optics with Anhui Institute of Optics and Fine Mechanics, Chinese Academy of Sciences, (AIOFM/CAS), Hefei, China, in 1995, and the Ph.D. degree in atmospheric physics with the Institute of Atmospheric Physics, Chinese Academy of Sciences (IAP/CAS), Beijing, China, in 1998.

He is with the Deputy Director–General of National Satellite Meteorological Center (NSMC/CMA) since 2013, the Chief Director of FY-3 ground segment since 2013, the Chair of Global Space Inter-Calibration System (GSICS) Executive Panel from 2014 to 2017, the Chief Director of Chinese TanSat satellite ground segment since 2015. His major field focuses on the atmospheric remote sensing, satellite data assimilation, satellite calibration and validation. He has the intensive experience in conceiving, developing, and operating FY-3 satellite ground segment.

Yanmeng Bi received the Ph.D. degree in atmospheric physics science from Peking University, Beijing, China, in 2006.

He is a member of the TanSat Team with the National Satellite Meteorological Center, Beijing, where he is responsible for the preprocessing of TanSat data. His research interests include remote sensing of CO2 from satellite.

Cheng Liu received the Ph.D. degree in environmental physics from the University of Heidelberg, Heidelberg, Germany, in 2010.

He was a Post-Doctoral Researcher at Harvard University, Cambridge, MA, USA. Since 2015, he has been a Professor with the University of Science and Technology of China, Hefei, China. His research interests include the remote sensing of air pollution gases and greenhouse gases from satellite and ground-based observations.

Youwen Sun received the Ph.D. degree from the Anhui Institute of Optics and mechanics, Hefei Research Institute, Chinese Academy of Sciences, Hefei, China.

He is an Associate Researcher with the Anhui Institute of Optics and mechanics, Hefei Research Institute, Chinese Academy of Sciences. His research interests are the detection and analysis of multicomponent pollution gases emitted by industrial pollution sources, portable remote sensing of greenhouse gas ground, high-precision Fourier transform spectral ground-based remote sensing of key atmospheric components, and long-term observation.

Wei Wang received the Ph.D. degree from the University of Science and Technology of China, Hefei, China, in 2013.

She is an Associate Professor with the Anhui Institute of Optics and Fine Mechanics, Chinese Academy of Sciences, Hefei. Her research interest includes the remote sensing of Atmospheric trace gases.

Zeqing Chen received the B.S. degree from China University of Geosciences, Wuhan, China, in 2017. She is pursuing the M.S. degree with the School of Earth and Space Sciences, University of Science and Technology of China, Hefei, China.

Her research interest includes the remote sensing of air pollution.

Hao Yin is pursuing the Ph.D. degree with the Anhui Institute of Optics and mechanics, Science Island branch, University of Science and Technology of China, Hefei, China.

His research interests are mainly in the research and long-term monitoring of high-precision Fourier transform spectral inversion method for key gas components in the atmosphere, the detection and analysis of gas emissions from various pollution sources, and the simulation of GEOS-Chem model.

Chengxin Zhang received the B.Eng. degree in automation and the Ph.D. degree in atmospheric remote sensing from the University of Science and Technology of China (USTC), Hefei, China, in 2015 and 2020, respectively.

He is a Post-Doctoral Researcher with USTC. His research interests include atmospheric optics and satellite remote sensing.

Yuan Tian received the Ph.D. degree from the University of Chinese Academy of Sciences, Hefei, China, in 2018.

She is a Lecturer with the Institutes of Physical Science and Information Technology, Anhui University, Hefei. Her research interests include satellite remote sensing and emission fluxes.

Jianguo Liu received the Ph.D. degree from the Anhui Institute of Optics and Fine Mechanics, Chinese Academy of Sciences, Hefei, China, in 1999.

He is the Deputy President with the Hefei Institutes of Physical Science, Chinese Academy of Sciences, and also the Director of the Key Laboratory of Environmental Optics and Technology. His research interest includes the optical environment pollution monitoring technology.